


Characterization of Titanium Lattice Structures Fabricated by Selective Laser Melting Using an Adapted Compressive Test Method

S.L. Sing^{1,2}  · W.Y. Yeong^{1,2} · F.E. Wiria^{1,3} · B.Y. Tay^{1,3}

Received: 6 July 2015 / Accepted: 1 December 2015 / Published online: 12 January 2016
© Society for Experimental Mechanics 2016

Abstract This paper investigates the effect of designs and process parameters on the dimensional accuracy and compressive behavior of cellular lattice structures fabricated using selective laser melting (SLM). Two unit cell types, square pyramid and truncated cube & octahedron from the Computer Aided System for Tissue Scaffolds (CASTS), an in-house developed library system were used. Powder adhesions occur on the struts of the lattice structures. The thickness of powder adhesion on the struts decreases with an increase in laser power or laser scan speed. The elastic constant in compression of the lattice structures increases with an increase in relative density, and ranged from 7.93 ± 2.73 MPa to 7.36 ± 0.26 GPa. Analysis of Variance (ANOVA) is also carried out to determine the significance of various process and design parameters on the dimensional accuracy and compressive strength of the lattice structures. The processing parameters, such as laser power and laser scan speed have no significant effect on the elastic constant but have a significant effect on the powder

adhesion on the struts, which in turn, affects the dimensional accuracy. However, geometrical design parameters such as unit cell type and strut diameter have significant effects on the elastic constant but not dimensional accuracy of the lattice structures.

Keywords Additive manufacturing · 3D printing · Rapid prototyping · Selective laser melting · Titanium · Statistical analysis

Introduction

Additive manufacturing (AM) refers to a group of techniques that fabricate part directly layer by layer. These technologies are poised to influence new designs and new applications in multiple fields such as aerospace [1], automotive [2], biomedical [3–7], electronics [8] and even consumer goods such as fashion and jewelry [9]. Selective laser melting (SLM) is one of these technologies that can be used to produce fully functional metallic parts directly [10–12]. The SLM process begins with splitting a component into layers and each of those layers is built on top of each other and fused together, layer after layer, by a laser power source until the part is fully formed [13, 14]. Rather than being sintered, the powders are melted completely which gives parts that are fully dense [11]. One of the key advantages of SLM is the ability to manufacture parts with complex geometries and lightweight structures, such as cellular lattice structures. Lattice structures can offer high performance, such as high strength to weight ratio, good thermal and acoustic insulation which makes them suitable for high value industrial applications such as aerospace and medical [15].

Titanium and its alloys are commonly used as biomaterials for implants due to their high biocompatibility and corrosion resistance [16]. However, like other metallic biomaterials, titanium has elastic moduli higher than that of human bones.

✉ W. Y. Yeong
wyyeong@ntu.edu.sg

S. L. Sing
sing0011@e.ntu.edu.sg

F. E. Wiria
florencia@simtech.a-star.edu.sg

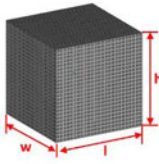
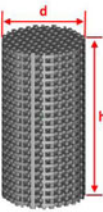
B. Y. Tay
bytay@simtech.a-star.edu.sg

¹ SIMTech-NTU Joint Laboratory (3D Additive Manufacturing), Nanyang Technological University, HW3-01-01, 65A Nanyang Drive, Singapore 637333, Singapore

² Singapore Centre for 3D Printing, School of Mechanical & Aerospace Engineering, Nanyang Technological University, HW1-01-05, 2A Nanyang Link, Singapore 637372, Singapore

³ Singapore Institute of Manufacturing Technology, 71 Nanyang Drive, Singapore 638075, Singapore

Table 1 Test parameters used in compression tests for cellular lattice structures

Sample shape	Sample dimensions (mm)	Strain rate (/min)	Reference
	$l = 25, w = 25, h = 15$	0.0267	[1, 15]
	$l = 14, w = 14, h = 24.5$	0.0408	[20]
	$d = 6, h = 12$	0.0167	[19]
	$d = 10, h = 17$	0.1059	[21]

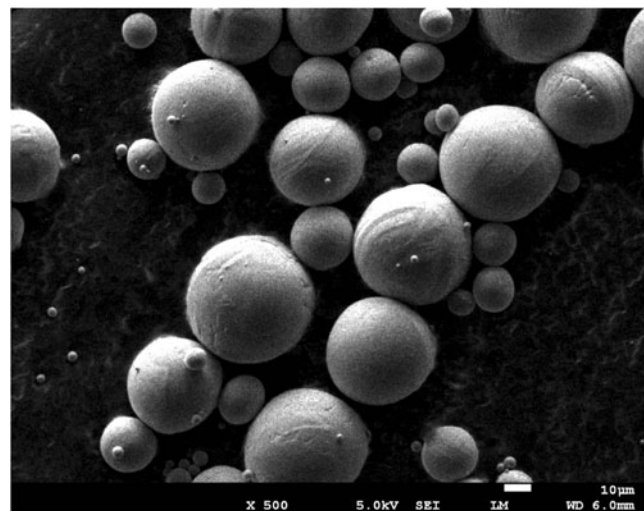
Human bones have wide range of elastic constants, for example from 6.9 GPa to 25.0 GPa [17], however, for commercially pure titanium fabricated by SLM, elastic constants can be 100 GPa [6]. This mismatch in modulus can result in an adverse effect called “stress shielding” [18]. “Stress shielding” induces an unfavorable stress distribution at the bone-implant interface, resulting in slower bone healing and remodeling [7, 18]. Through the introduction of porosity by creating lattice structures, it is possible to minimize this adverse effect *via* the reduction of elastic moduli of the implants. By using SLM, there is greater liberty in designing porosity on the implants.

Various studies have been conducted in the fabrication of cellular lattice structures using SLM. This process has shown great potential in this area. Yan et al. evaluated the manufacturability and performance of SLM produced periodic cellular lattice structures, which are designed using a repeating unit called gyroid consisting of circular struts and a spherical core. The effect of unit cell size on the manufacturability, density and compression properties of the manufactured structures was

investigated [1, 15]. Van Bael et al. evaluated the robustness and controllability of the production of porous Ti6Al4V structures by comparing the fabricated parts to the design, in terms of pore size, strut thickness, porosity, surface area and structure volume [19]. Lin et al. investigated the radiographic characteristics and mechanical properties of a topologically optimized lumbar interbody fusion cage made of Ti6Al4V by SLM [20]. Despite the studies conducted, there is limited information on the effect of design and processing parameters of SLM on the quality and mechanical properties of cellular lattice structures.

Table 2 Standard test parameters and sample designs

Standard	Sample shape	Sample dimensions ratio	Strain rate (/min)
ASTM E9	Cylinder	1.5 or 2	0.005
ISO 13314-2011	Cylinder cube	Between 1 and 2	Between 0.06 to 0.6

**Fig. 1** SEM micrograph of the cpTi powder

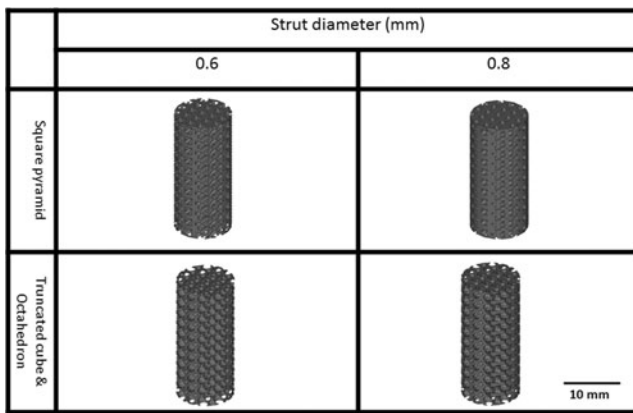


Fig. 2 CAD files for fabrication by SLM

Various research groups have also carried out compression tests on cellular lattice structures fabricated by SLM. It was found that the design of test such as sample shape, sample dimensions and compressive deformation rate used in these works were not standardized. The variations of compressive test method reported are tabulated in Table 1 [1, 15, 19–21].

There are differences in the design of the test samples and method as there is no additive manufacturing specific standards in this area. Furthermore, all of these published works differ from ASTM E9 and/or ISO 13314–2011. According to the standards, cylinder samples are recommended, although the ISO standard also allows samples with rectangular cross sections. For the published work that used cylinder samples, the deformation rates deviate from both standards, without any rationale stated.

The compressive deformation rate has to be set such that the strain rate experienced by the samples are constant throughout. The compressive deformation rate and strain rate is related by the following equation:

$$\text{strain rate} = \frac{\text{compressive deformation rate}}{\text{height of test sample}}$$

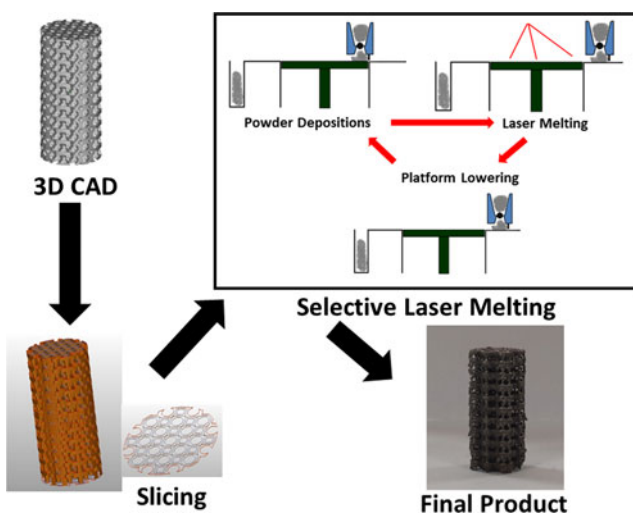


Fig. 3 Schematic of SLM process in fabrication of lattice structures

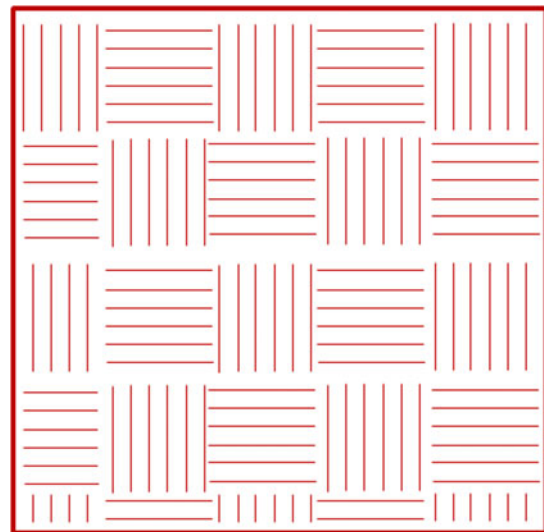


Fig. 4 Chessboard scanning strategy used in SLM

Using a standardized strain rate minimizes the differences in results obtained due to the effect of strain rate on hardening behavior which may be present in some materials [22–25]. The recommended strain rate in ASTM E9 is 0.005 /min, however, ISO-13314-2011 stated a range of strain rates between 10^{-3} /s and 10^{-2} /s (0.06 and 0.6 /min). The difference in strain rates recommended may be due to ASTM E9 standard is designed from solid while ISO 13314–2011 is designed for porous structures. The test parameters from ASTM E9 and ISO 13314–2011 is listed in Table 2.

In this paper, the feasibility of adapting ASTM E9 standard for compression testing on cellular lattice structures fabricated by SLM was studied. The effect of processing parameters and geometrical designs on the dimensional accuracy and the compressive behavior of cellular lattice structures fabricated using SLM are also investigated. Dimensional accuracy of the SLM process affects the mechanical properties of the lattice structures fabricated. From the compression tests, the elastic constant of the lattice structures generated can be determined to evaluate the suitability of these designs for implants applications. Analysis of variance (ANOVA) is carried out to determine the significance of various processes and design parameters on the dimensional accuracy and compressive strength of the lattice structures.

Experimental Details

Materials

The cellular lattice structures were fabricated using commercially pure titanium (cpTi, ASTM B348 grade 2, LPW Technology Ltd, UK) gas atomized powder with particle size

Table 3 Factors considered in experiment design

Factor		Level	
		High (+)	Low (-)
A	Unit cell geometry	Square pyramid	Truncated cube & octahedron
B	Strut diameter (mm)	0.8	0.6
C	Laser power (W)	360	240
D	Laser scan speed (mm/s)	800	400

distribution of 5 to 40 μm . The scanning electron microscope (SEM) image of the cpTi powder is shown in Fig. 1.

Design of Cellular Lattice Structures

The computer aided design (CAD) models of the cellular lattice structures were designed and generated using Computer Aided System for Tissue Scaffolds (CASTS), the in-house developed library system consisting of 13 different polyhedral units that can be assembled into scaffold structures using programmed algorithms [3, 26]. The polyhedral units chosen for this study were square pyramid and truncated cube & octahedron [26]. The dimensions of the repeating unit cell were 1 mm by 1 mm by 1 mm. The detailed illustrations of CASTS have been described by Naing et al. and Chua et al. [27, 28].

The generated CAD models are shown in Fig. 2.

Selective Laser Melting

The fabrication of the samples was carried on a SLM 250HL machine made by SLM Solutions Group AG, Germany. The detailed process sequence is shown in Fig. 3.

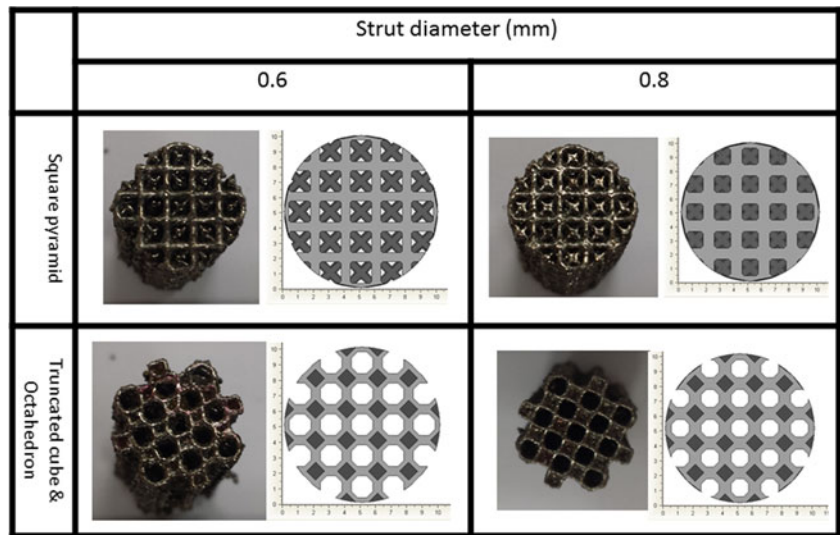
Using the CAD files generated, the 3D models are then sliced into layers of predetermined thickness. During the SLM process, the laser scans and selectively melts deposited titanium powder based on the cross-section of these slices. Once the cross-section is scanned completely, the mechanical building platform lowers by the same amount as the thickness of the slices and a new powder layer is deposited. This is then followed by laser melting of selective area again. The process cycle continues and repeats until the 3D part is formed fully based on the CAD model. The parts can then be removed from the platform and used directly.

The SLM machine is equipped with a Gaussian beam fiber laser of power up to 400 W with a focus diameter of 80 μm . All processes occurred in an argon environment with less than 0.05 % oxygen. This prevents oxidation and material degradation by pick up of interstitial elements such as oxygen and nitrogen during the process. Any chemical reaction between the molten material and the surrounding environment during the process is restricted [11]. This work used sectorial (island or chessboard) scanning strategy during the SLM process [29, 30]. The scanning strategy is shown in Fig. 4. This scanning

Table 4 Parameters of the lattice structures fabricated by SLM

Specimens	Unit cell geometry	Strut diameter (mm)	Laser power (W)	Laser scan speed (mm/s)
1	Square pyramid	0.6	240	400
2			800	
3			360	400
4			800	
5		0.8	240	400
6			800	
7			360	400
8			800	
9	Truncated cube & octahedron	0.6	240	400
10			800	
11			360	400
12			800	
13		0.8	240	400
14			800	
15			360	400
16			800	

Fig. 5 Top view of the as fabricated samples with their corresponding CAD image



strategy has been reported to minimize thermal stresses formed during the process [29, 30].

Design of Experiment Using Analysis of Variance

A 2⁴ factorial design is chosen by disregarding the porosity of the lattice structures and the hatch spacing during the SLM process. The factors and their two levels for the 2⁴ factorial design are listed in Table 3.

The particular laser powers and scan speeds were chosen because these combinations of parameters can produce bulk cpTi samples of relative density close to 100 % in preliminary experiments, compared to theoretical density of cpTi (4.51 g/cm³).

Based on the design of experiment, the following lattice structures described in Table 4 were fabricated by SLM for ANOVA.

ANOVA uses a test statistics called the F statistic to test the null hypotheses. From the F distribution table, with

probability of 1 % in which the null hypothesis is rejected when it is actually true, *i.e.*, the factor is concluded that it is significant when it is not, the control limit F value is 16.26. If the F₀ value of factor A (Unit cell geometry), B (Strut diameter), C (Laser power) or D (Laser scan speed) is higher than the control limit, the ANOVA results indicate that the respective factor is significant in affecting the results.

Mechanical Characterization

The fabricated samples are cylindrical and have designed height of 22 mm and diameter of 10 mm, which are used as test coupons for compression tests based on ASTM E9 which recommended that compression test specimens be in the form of solid circular cylinders, where feasible. The length to diameter ratio of close to 2 is best adapted for high strength materials according to ASTM E9.

Uni-axial compression tests were carried out, at room temperature (25 °C), to assess the compressive properties of the

Fig. 6 Side view of the as fabricated samples with their corresponding CAD image

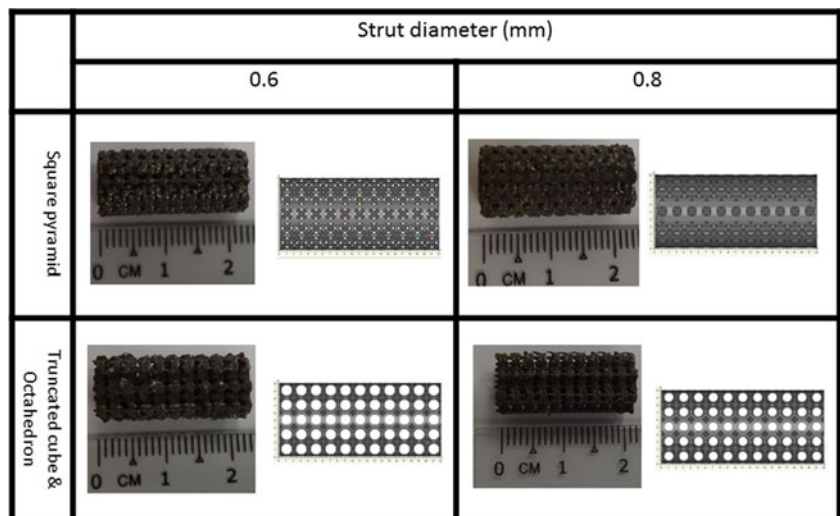
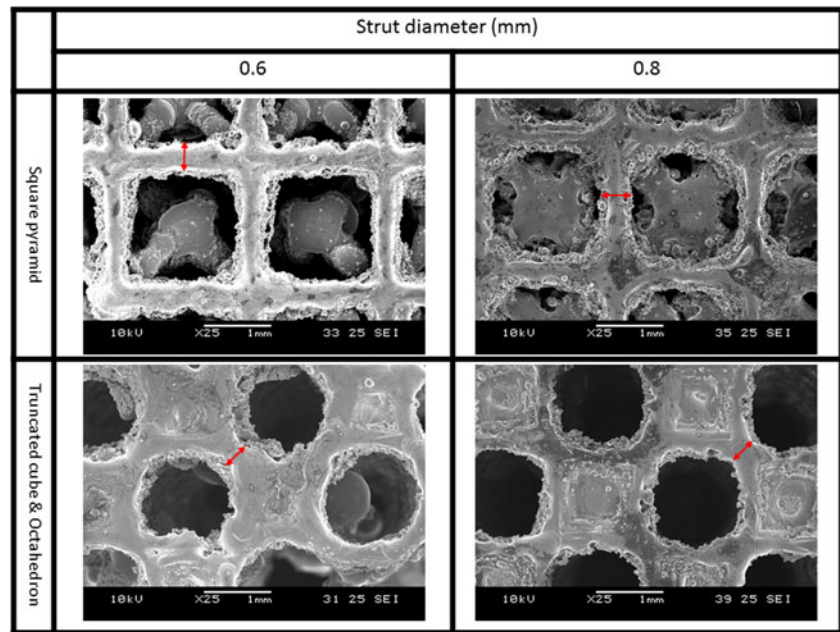


Fig. 7 SEM images of fully formed struts



lattice structures, each with 3 replicates, by using Instron Static Tester Series 5569 (Instron, United States) equipped with a 50 kN load cell. The loading speed was set at a constant of 0.4 mm/min, so as to maintain a constant strain rate for all tests as recommended by ASTM E9. The loading rate (compressive deformation rate) gives a strain rate of 0.02 /min. The strain rate is chosen not to follow ASTM E9 as due to the short height of the samples, since setting the strain rate in accordance to ASTM E9 will result in a low loading speed of 0.1 mm/min. A low loading speed is not recommended due to the high percentage fluctuations of the mechanical component of the tester during the tests. A high strain rate recommended by ISO-13314-2011 can lead to abnormal strain hardening behavior in titanium [22–24]. To ensure consistency, the test samples are all strained at a uniform rate, without sudden changes, to minimize the effects of different strain rates [23, 24, 31].

The compression tests were carried out until axial deformation of the samples was equal to 50 % or when the maximum loading of 50 kN was reached, whichever came first. The

stress–strain curves and elastic constants in compression of the as-fabricated samples were then obtained through the compression tests. The as-fabricated samples replicate the shapes of the CAD files designed for this experiment, as shown in Figs. 5 and 6. The samples show that the designed CAD models can be fabricated successfully using SLM.

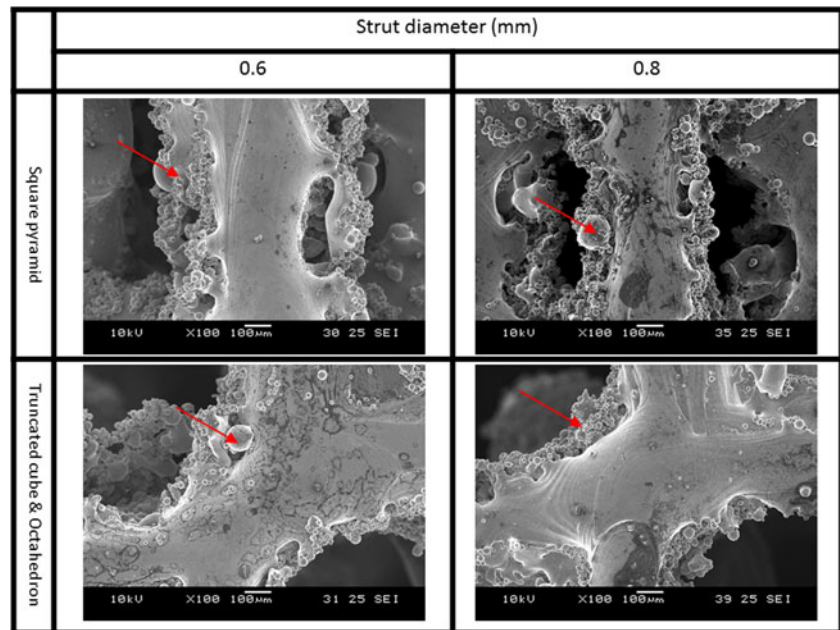
Metrological Characterization

The overall dimensions of the as-fabricated lattice structures were measured using digital Vernier calipers of 0.01 mm accuracy (ABS Digimatic Calipers, Mitutoyo Corporation, Japan). The sample dimensions were derived from the average of 3 points on each of the 3 replicates of the as-fabricated samples. The struts of the as-fabricated samples underwent micro-morphological characterization using JSM-5600LV Scanning Electron Microscope (JEOL Ltd, Japan). The same equipment was also used for measurement of the strut size using

Table 5 Strut diameter of lattice structures

Laser power (W)	Scanning speed (mm/s)	Actual strut diameter (mm)			
		Square pyramid		Truncated cube & octahedron	
		Designed strut diameter 0.6 mm	Design strut diameter 0.8 mm	Designed strut diameter 0.6 mm	Designed strut diameter 0.8 mm
240	400	0.255 ± 0.083	0.222 ± 0.132	0.263 ± 0.146	0.282 ± 0.116
240	800	0.212 ± 0.092	0.206 ± 0.084	0.208 ± 0.053	0.217 ± 0.061
360	400	0.152 ± 0.091	0.186 ± 0.090	0.177 ± 0.114	0.201 ± 0.068
360	800	0.135 ± 0.073	0.122 ± 0.072	0.165 ± 0.088	0.145 ± 0.055

Fig. 8 SEM images showing powder adhesions on the struts



the SEM images. The strut diameters were measured based on the fully formed strut, without taking into consideration of powder adhesion to the struts, which will be discussed later in this paper. For every SEM image, 10 values of the strut size were measured and the average value was taken. A similar method was used to measure the powder adhesion thickness on the struts.

Results and Discussion

Dimensional Accuracy

The built samples have an average height of 21.86 ± 0.11 mm and diameter of 9.99 ± 0.09 mm. The results show that, in term of diameters, the SLM process have high accuracy (shown by the average value which is closed to the designed 10 mm) and high precision (shown by the small standard deviation). However, the individual samples may deviate slightly from the designed value because the laser scan area was set with a contour spacing of 0.13 mm which may attribute to a tolerance of similar value. In general, the samples are shorter than the designed height. This can be attributed to the electrical discharge machining (EDM) wire cut employed to remove the samples fabricated from the substrate plate. The actual test samples did not follow the standardized geometry outlined in ASTM E9 and ISO 13314–2011, however, they are consistent with each other, which will eliminate any variation in results due to height difference from the specified values of the standards.

Figure 7 show the SEM images of the as-fabricated samples with different designs and process parameters. Sample

measurements of strut diameters were also marked in red in the figures. It is observed that the struts of the lattice structures are solid, connected and continuous, indicating good melting of the powder during the SLM process. The variation between the strut designs in CAD and the actual struts may be due to the laser power fluctuations during the SLM process.

The actual strut diameters of square pyramid and truncated cube & octahedron lattice structures are shown in Table 5.

The experimental strut diameters are found to be smaller than the designed values of 0.6 and 0.8 mm. The smaller experimental strut diameters compared to the designed value can be attributed to the following reasons. Firstly, the CAD is sliced and scanned using the designed scan strategy with a contour spacing of 0.13 mm. The contour scan results in partially melted metal

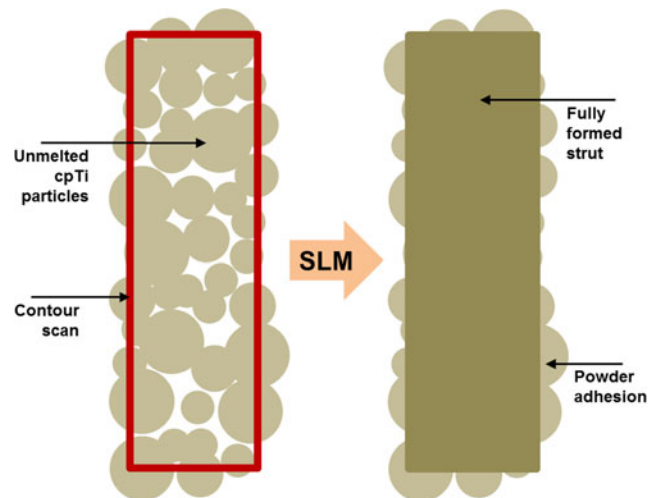


Fig. 9 Schematic of formation of powder adhesions on the struts

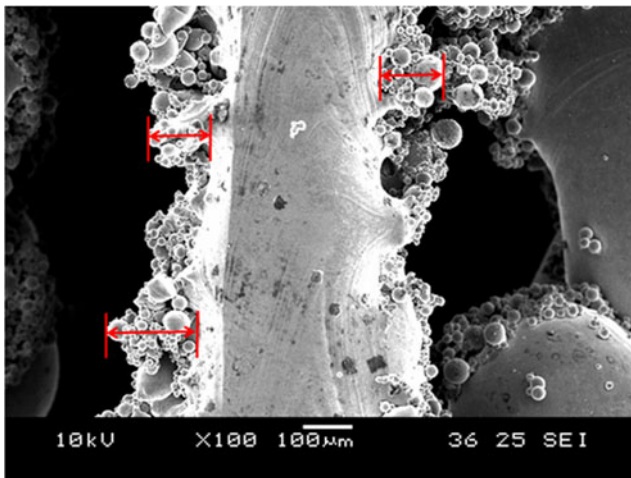


Fig. 10 Thickness of powder adhesions on struts

particles bonded onto the struts, instead of forming the continuous struts. Powder adhesions onto the strut are shown in Fig. 8. Secondly, the melt pool size of the scan vectors did not reach the boundaries of a strut as the laser spot size of 80 μm is smaller than input hatch spacing of 0.1 mm.

The results obtained contradict some of the findings made when porous metal structures were manufactured by SLM done by other groups. Yan et al. found the strut sizes of the SLM-manufactured gyroid lattice structures were higher than the designed value [15]. Van Bael et al. evaluated the Ti6Al4V porous structure fabricated by SLM through micro-CT image analysis and reported the increase in strut size compared to the designed value [19]. The contradiction between the results occurred because the other groups considered the powder adhered to the struts as part of the struts, however, powder that are not melted behave differently from SLM processed metal, especially under compression loading. Hence, the adhered powder is not regarded as part of the struts in this study.

From Fig. 8, it can be observed that there are a lot of adhered powder particles on the struts of the lattice structures. Similar phenomenon has also been observed in the titanium porous structures fabricated using SLM by Pattanayak et al. [13]. The presence of these particles on the struts may be due

to partial melting phenomenon of the raw titanium particles on the boundary of the solid struts due to the contour laser track, which was only scanned once. These partially melted particles then adhere to the fully formed struts that underwent repeated melting due to the melt pool overlap as a result of hatch spacing setting. A schematic explaining the formation of powder adhesion on the struts is shown in Fig. 9.

Heat treatment can be carried out to make the partially melted titanium particle fuse and bond with the laser melted strut, thus, increasing the dimensional accuracy [13]. Due to powder adhesion on the struts of lattice structures, different set of parameters may be required for fabrication as compared to fabrication of parts with bigger cross sections.

The actual amount of powder adhesion is quantified by measuring the thickness of partially melted particles adhered to the struts as shown in Fig. 10.

The resulting powder adhesion thicknesses of square pyramid and truncated cube & octahedron lattice structures are shown in Table 6.

It can be observed that at fixed laser power, the powder adhesion thickness on the struts decreases with increasing scanning speed. At higher scanning speed, the energy transferred to the powder particles is lower, resulting in lesser partially melted powder particles formed during the contour scan of the struts, which decreases powder adhesions around the struts. This finding coincides with the results obtained by parametric study done by Loh *et al.* on width of single melt track during SLM process [32].

At a fixed scan speed, the powder adhesion thickness on the struts decreases with an increase in laser power. At higher laser power, the energy transferred to the powder particles is higher during the contour scan, resulting in more fully melted powder particles forming the struts, which results in lower powder adhesions around the struts. In addition, surrounding powder particles may have evaporated at higher laser power due to the higher energy transferred to them, resulting in temperatures that exceed boiling point of cpTi. Evaporated particles are blown away by the flow of argon gas during the SLM process.

Fluctuations in the thickness of powder adhesion, even within a single strut, are observed. This is due to the inherent

Table 6 Powder adhesion thickness of lattice structures

Laser power (W)	Scanning speed (mm/s)	Powder adhesion thickness (mm)			
		Square pyramid		Truncated cube & octahedron	
		Designed strut diameter 0.6 mm	Design strut diameter 0.8 mm	Designed strut diameter 0.6 mm	Designed strut diameter 0.8 mm
240	400	0.433 ± 0.042	0.532 ± 0.07	0.550 ± 0.045	0.472 ± 0.048
240	800	0.335 ± 0.026	0.335 ± 0.042	0.446 ± 0.022	0.364 ± 0.026
360	400	0.388 ± 0.054	0.361 ± 0.021	0.433 ± 0.035	0.454 ± 0.036
360	800	0.370 ± 0.038	0.325 ± 0.031	0.342 ± 0.032	0.380 ± 0.029

Table 7 Table of ANOVA for powder adhesions of the lattice structures

Source of variation	Sum of squares	Degrees of freedom	Mean square	F ₀
A	1.76×10^{-3}	1	1.76×10^{-3}	5.24
B	1.22×10^{-5}	1	1.22×10^{-5}	0.04
C	2.12×10^{-2}	1	2.12×10^{-2}	62.84
D	6.72×10^{-3}	1	6.72×10^{-3}	19.96
AB	1.56×10^{-4}	1	1.56×10^{-4}	0.46
AC	2.03×10^{-5}	1	2.03×10^{-5}	0.43
AD	1.44×10^{-4}	1	1.44×10^{-4}	0.06
BC	8.10×10^{-5}	1	8.10×10^{-5}	0.24
BD	3.42×10^{-4}	1	3.42×10^{-4}	1.31
CD	5.63×10^{-5}	1	5.63×10^{-5}	1.02
ABC	4.41×10^{-4}	1	4.41×10^{-4}	0.21
ABD	7.22×10^{-5}	1	7.22×10^{-5}	0.17
ACD	3.42×10^{-4}	1	3.42×10^{-4}	1.02
BCD	7.29×10^{-4}	1	7.29×10^{-4}	2.16
ABCD	1.00×10^{-4}	1	1.00×10^{-4}	0.30
Error	1.68×10^{-3}	5	3.37×10^{-4}	
Total	3.22×10^{-2}			

fluctuation of the power of the laser module in the SLM machine, even during continuous scan of a single strut. Furthermore, the powder used has a range of sizes which will also result in variation in the thickness of powder adhesion.

Analysis of variance

The analysis of variance (ANOVA) was performed to evaluate the factors with significant effects on the thickness of powder adhesion on the struts. The results of the ANOVA is shown in Table 7.

Since only the F₀ value of factor C (62.84) and D (19.96) are higher than the control limit (16.26), the ANOVA results indicate that out of the four factors, only laser power and laser scan speed are significant factors that affect the thickness of powder adhesion on the struts of the lattice structures. Design

parameters, such as unit cell geometry and strut diameter, do not have a significant effect on the thickness of powder adhesion on the struts of the lattice structures.

From ANOVA, it has also been proven statistically that laser power has the most significant effect on thickness of the powder adhesion on the struts of lattice structures. This finding is in agreement with the results obtained from the parametric study done by Loh et al. which states that a change in laser power has a larger effect on the melt width than a change in laser scan speed [32].

Compressive Properties

The resulting elastic constant in compression of square pyramid and truncated cube & octahedron lattice structures are shown in Table 8. The slope of the straight-line portion of the stress–strain curve is established to define the elastic constant. The standard variations in the elastic constant may be due to the varying amount of powder adhesion on the struts which in turn, affects the compressive properties of the lattice structures.

In order to determine the repeatability of the sample and test design chosen, the coefficient of variance (COV) for elastic constant in compression of all the samples are calculated and tabulated in Table 9.

It is determined that the COV of all the data sets are low (less than 1), which indicates good repeatability of the test method designed.

In general, the lattice structures fabricated using the square pyramid unit cells have higher elastic constants than the lattice structures of truncated cube & octahedron unit cells. This is because the designed and actual porosity of the square pyramid unit cells is lower than that of the truncated cube & octahedron unit cells, as shown in Table 10. The designed porosities are obtained by comparing the volume of CAD models of a full dense cylinder and the lattices structures. The experimental porosities are obtained by density measurements of the lattice structures and comparing it to theoretical density of cpTi, which is 4.51 g/cm³.

Table 8 Elastic constant of lattice structures

Laser power (W)	Scanning speed (mm/s)	Elastic constant (GPa)			
		Square pyramid		Truncated cube & octahedron	
		Designed strut diameter 0.6 mm	Design strut diameter 0.8 mm	Designed strut diameter 0.6 mm	Designed strut diameter 0.8 mm
240	400	1.170±0.158	7.358±0.257	0.112±0.046	0.276±0.029
240	800	0.422±0.113	4.087±0.299	0.316±0.101	0.305±0.036
360	400	0.450±0.102	4.210±0.428	0.0547±0.040	0.268±0.064
360	800	0.838±0.165	2.534±0.140	0.008±0.002	0.250±0.011

Table 9 Coefficient of variance of elastic constant of lattice structures

Laser power (W)	Scanning speed (mm/s)	Coefficient of variance			
		Square pyramid		Truncated cube & octahedron	
		Designed strut diameter 0.6 mm	Design strut diameter 0.8 mm	Designed strut diameter 0.6 mm	Designed strut diameter 0.8 mm
240	400	0.135	0.035	0.411	0.105
240	800	0.268	0.073	0.320	0.118
360	400	0.227	0.102	0.731	0.239
360	800	0.197	0.055	0.250	0.044

Due to the design flexibility of the lattice structures, the elastic constant of the lattice structures can range from 7.93 ± 2.73 MPa to 7.36 ± 0.26 GPa. This shows the versatility of design of cpTi lattice structures in various applications, especially for orthopedic implants where bones have wide range of elastic constants, for example from 6.9 GPa to 25.0 GPa [17]. Therefore, the lattice structure design for both model and strut size can be adjusted according to the various needs of an orthopedic implant. This is one of the pronounced advantages of using an additive manufacturing technology to fabricate orthopedic implants.

Using the Gibson–Ashby model [33], the compressive modulus at different relative densities can be estimated as follows,

$$\frac{E}{E_0} = C_1 \left(\frac{\rho}{\rho_0} \right)^2$$

where E and ρ are the apparent Young's modulus and density of the lattice structures, E_0 and ρ_0 are the elastic modulus, density of fully dense material, respectively.

Bulk compressive elastic modulus of cpTi is taken from the fabricated fully dense cylinders. Hence, $E_0 = 16.66 \pm 1.93$ GPa. C_1 is a constant that can be calculated based on the compression test results after fitting the suggested formula. In this study, C_1 was calculated to be 0.377 and 0.206, for the

square pyramid and truncated cube & octahedron unit cells, respectively. The experimental values of Young's modulus and the theoretical values based on the Gibson–Ashby model is tabulated and plotted in Table 11 and Fig. 11.

It is observed that the compressive modulus of the as-fabricated lattice structures increases with an increase in relative density, which is consistent with the prediction from the Gibson–Ashby model. From Fig. 11, it can be seen that there are differences between experimentally tested and Gibson–Ashby model estimated Young's modulus. The differences between the theoretical and experimental values may be attributed to the residual stress inherent due the SLM process, waviness and roughness of the strut surfaces [1]. It can also be due to the disregard of the SLM process parameters and geometrical shapes of unit cells of the lattice structures by the Gibson–Ashby model. The model also disregards the powder adhesion on the strut which will affect the compressive properties of the lattice structures and failed to take into account the type of failure underwent by the lattice structures.

For the square pyramid lattice structures, the typical stress–strain curve is plotted in Fig. 12. The graph is plotted using result from 0.6 mm strut diameter specimen, fabricated with 240 W laser power and 400 mm/s scanning speed.

Table 10 Designed and experimental porosity of lattice structures

Laser Power (W)	Scanning Speed (mm/s)	Porosity							
		Square pyramid				Truncated cube & octahedron			
		Designed strut diameter 0.6 mm		Designed strut diameter 0.8 mm		Designed strut diameter 0.6 mm		Designed strut diameter 0.8 mm	
		Designed	Experimental	Designed	Experimental	Designed	Experimental	Designed	Experimental
240	400	0.532	0.549 ± 0.005	0.306	0.413 ± 0.009	0.804	0.716 ± 0.001	0.754	0.809 ± 0.001
240	800		0.720 ± 0.037		0.393 ± 0.010		0.792 ± 0.003		0.768 ± 0.002
360	400		0.771 ± 0.001		0.380 ± 0.002		0.793 ± 0.002		0.773 ± 0.001
360	800		0.686 ± 0.030		0.393 ± 0.003		0.681 ± 0.013		0.832 ± 0.001

Table 11 Experimental and theoretical values of elastic constant

Unit cell geometry	Strut diameter (mm)	Gibson–Ashby model (GPa)	Experimental young’s modulus (GPa)
Square pyramid	0.6	1.376	0.687
	0.8	3.025	4.547
Truncated cube & octahedron	0.6	0.132	0.112
	0.8	0.208	0.238

It is observed that the stress–strain curve for square pyramid lattice structures shows an elastic region with a relative high degree of linearity (region A), followed by a second elastic region of lower degree of linearity (region B). This is due to the vertical and diagonal struts handling the load at the initial start of the loading, accounting for the first linear region. Buckling occurs from region B. When the vertical struts start to buckle, the loading is handled by only the diagonal struts of the lattice structure, accounting for the second linear region. The samples underwent permanent deformation after the compression. This behavior is also observed in lattice structures made of 316L stainless steel using SLM [15].

For the truncated cube & octahedron lattice structures, the typical stress–strain curve is plotted in Fig. 13. The graph is plotted using result from 0.8 mm strut diameter specimen, fabricated with 240 W laser power and 400 mm/s scanning speed.

It can be observed that the lattice structures made from the truncated cube & octahedron unit cells have an elastic deformation region (region A), follow by a plateau region in which the stress fluctuates (region B), and finally a densification region characterized by a rapid stress increase (region C). Buckling occurs from region B and stress fluctuation in this region is a characteristic of brittle fracture. This is in contrast with the square pyramid lattice structures which exhibit ductile behavior. The samples underwent permanent deformation and fracture after the compression. The brittle behavior is also observed in Ti6Al4V cellular structures fabricated by electron beam melting (EBM) [34].

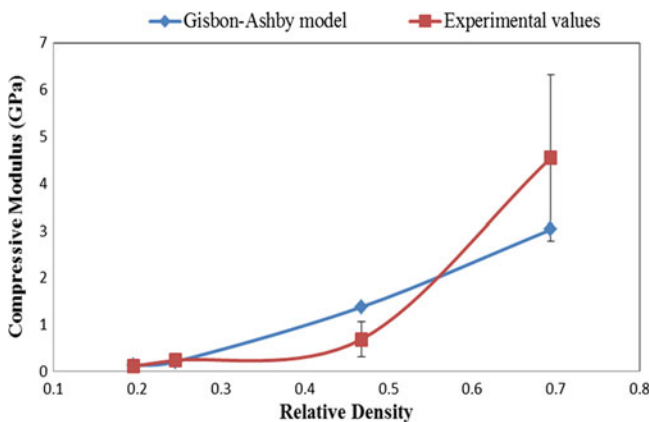


Fig. 11 Theoretical and experimental values of elastic constant

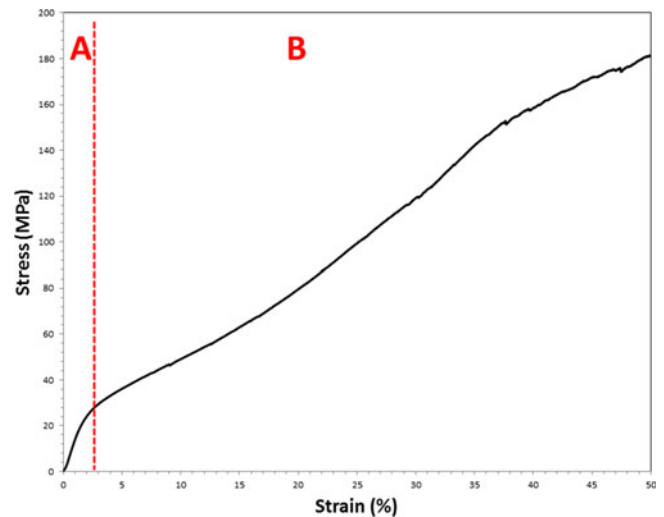


Fig. 12 Typical stress–strain curve for square pyramid lattice structures

The square pyramid and truncated cube & octahedron lattice structures exhibit the same shape of stress–strain curve respectively, as shown in Figs. 12 and 13, however, some differences such as different slope within the elastic region, can be identified within specimens of the same unit cells. The differences in the graph can be attributed to reasons such as difference in strut diameters as a results of the difference in processing parameters and designed values as discussed previously.

The difference in compression behavior of square pyramid and truncated cube & octahedron cellular lattice structures can also be observed from the compressed samples as shown in Fig. 14.

The ductile behavior of the square pyramid cellular lattices is characterized by a near-linear buckling of the samples shown by the linearity of the compressed shapes. However, the brittle behavior of truncated cube & octahedron cellular lattices are shown

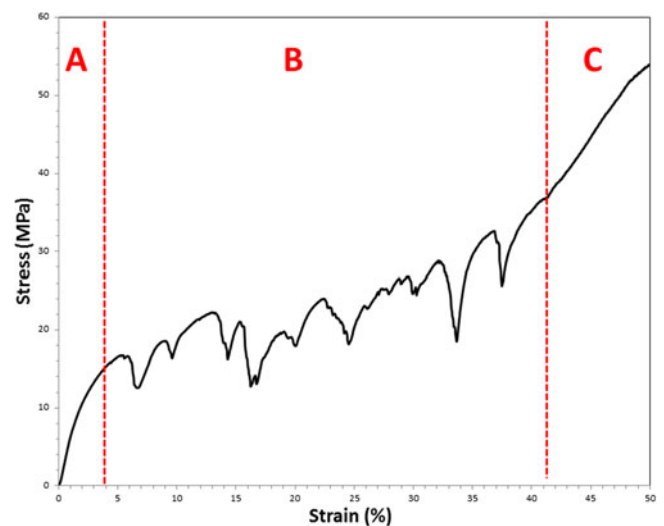
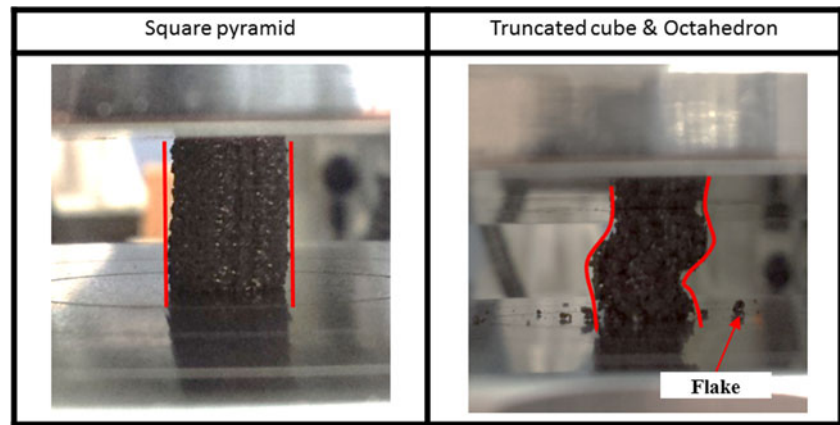


Fig. 13 Typical stress–strain curve for truncated cube & octahedron lattice structures

Fig. 14 Compressed samples of square pyramid and truncated cube & octahedron cellular lattice structures



by random buckling of the samples, characterized by the wavy buckling, and random flaking of the compressed shapes [35].

Analysis of variance

The analysis of variance (ANOVA) was performed to evaluate the factors with significant effects on elastic constant of the lattice structures. The results of ANOVA is shown in Table 12.

Since only the F_0 value of factor A (36.84) and B (24.60) are higher than the control limit (16.26), the ANOVA results indicate that out of the four factors, only cell geometry and strut diameter are significant factors that affect the elastic constant of lattice structures. SLM process parameters, such as laser power and laser scan speed, do not have a significant effect

Table 12 Table of ANOVA for compressive elastic modulus of the lattice structures

Source of variation	Sum of squares	Degrees of freedom	Mean square	F_0
A	2.37×10^7	1	2.37×10^7	36.84
B	1.58×10^7	1	1.58×10^7	24.60
C	1.85×10^6	1	1.85×10^6	2.87
D	1.65×10^6	1	1.65×10^6	2.56
AB	1.35×10^7	1	1.35×10^7	20.98
AC	1.31×10^6	1	1.31×10^6	2.91
AD	1.87×10^6	1	1.87×10^6	2.03
BC	1.05×10^6	1	1.05×10^6	1.63
BD	1.40×10^6	1	1.40×10^6	2.14
CD	3.70×10^5	1	3.70×10^5	2.18
ABC	1.38×10^6	1	1.38×10^6	1.92
ABD	1.23×10^6	1	1.23×10^6	0.57
ACD	5.74×10^5	1	5.74×10^5	0.89
BCD	2.77×10^4	1	2.77×10^4	0.04
ABCD	4.16×10^3	1	4.16×10^3	0.01
Error	3.22×10^6	5	6.44×10^5	
Total	6.58×10^7			

on the elastic constant of lattice structures. The insignificance of process parameters on compressive strength is also observed by Chlebus et al. [36].

From ANOVA, the interaction between cell geometry and strut diameter is also significant in affecting the elastic constant of the lattice structures. Both cell geometry and strut diameter affect the porosity of the lattice structures, which influences the elastic constant. It has also been proven statistically that cell geometry has the most significant effect on elastic constant of the structures.

Conclusion

This study investigates the feasibility of using adapted ASTM E9 for cellular lattice structures fabricated by SLM. The fabricated structures are also characterized mechanically and dimensionally. The lattice structures investigated are made of two types of unit cells, namely, the square pyramid and the truncated cube & octahedron unit cells. The major findings of this research are:

1. Test method from ASTM E9 can be adapted as a standardized test method for cellular lattice structures fabricated by AM or specifically, SLM. By using coefficient of variance, the repeatability of the adapted test method is shown.
2. It is observed that the struts of the lattice structures are solid, connected and continuous, indicating good melting of the powder during the SLM process.
3. The experimental strut diameters are found to be smaller than the designed values. The decrease in strut diameter compared to the designed value can be attributed to the scan strategy used which included the contour scan and powder adhesion that occurred during the process.
4. Due to the occurrence of powder adhesion on struts of lattice structures, different set of parameters, such as lower laser power and higher scanning speed, may be required for fabrication as compared to fabrication of parts with bigger cross sections. At a fixed scan speed, the thickness of powder adhesion on the struts decreases with an

increase in laser power. At fixed laser power, the thickness of powder adhesion on the struts decreases with an increase in scanning speed. Using ANOVA, it is concluded that the SLM processing parameters, such as laser power and laser scan speed, have significant effect on the powder adhesion thickness. However, design parameters such as unit cell geometry and strut diameter have no significant effect.

5. Compressive behavior of the lattice structures can be altered by the geometrical design. The square pyramid lattice structures exhibit ductile behavior under compression while the truncated cube & octahedron lattice structures have a brittle characteristic. Using ANOVA, it is concluded that the SLM processing parameters, such as laser power and laser scan speed, have no significant effect on the elastic constant of lattice structures. The elastic constant of lattice structures can be significantly altered with geometrical design of the unit cells as well as the strut diameters.

References

1. Yan C et al (2014) Advanced lightweight 316 L stainless steel cellular lattice structures fabricated via selective laser melting. *Mater Des* 55:533–541
2. Liu ZH et al (2014) Interfacial characterization of SLM parts in multi-material processing: Metallurgical diffusion between 316 L stainless steel and C18400 copper alloy. *Mater Charact* 94:116–125
3. Yeong WY et al. (2005) Development of scaffolds for tissue engineering using a 3D inkjet model maker. *Virtual Modelling and Rapid Manufacturing: Adv Res Virtual Rapid Prototyp* 115–118
4. Lee JM et al (2015) Characterization and Evaluation of Three-dimensional Printed Microfluidic Chip for Cell Processing. *Microfluidics and Nanofluidics* doi:10.1007/s10404-015-1688-8
5. Lee JM, Yeong WY (2014). A preliminary model of time-pressure dispensing system for bioprinting based on printing and material parameters. *Virtual Phys Prototyping* 10(1):3-8
6. Ng WL et al. (2014) Potential of bioprinted films for skin tissue engineering. *Proceedings of the 1st International Conference on Progress in Additive Manufacturing* 441–446
7. Heinl P et al (2008) Cellular Ti-6Al-4 V structures with interconnected macro porosity for bone implants fabricated by selective electron beam melting. *Acta Biomater* 4(5):1536–1544
8. Sing SL et al (2015) Interfacial characterization of SLM parts in multi-material processing: Intermetallic phase formation between AlSi10Mg and C18400 copper alloy. *Mater Charact* 105:220–227
9. Yap YL, Yeong WY (2014) Additive manufacturing of fashion and jewellery products: a mini review. *Virtual Phys Prototyping* 9(3): 195–201
10. Sing SL et al. (2013) Classical lamination theory applied on parts produced by selective laser melting. *High Val Manufac: Adv Res Virtual Rapid Prototyp* 77–82
11. Loh LE et al (2014) Selective laser melting of aluminium alloy using a uniform beam profile. *Virtual Phys Prototyping* 9(1):11–16
12. Sing SL, Yeong WY, Wiria FE et al. (2016) Selective laser melting of titanium alloy with 50 wt% tantalum: Microstructure and mechanical properties. *J Alloys Compounds* 660:461–470
13. Yasa E et al (2010) Charpy impact testing of metallic selective laser melting parts. *Virtual and Phys Prototyping* 5(2):89–98
14. Sing SL et al. (2015) Laser and electron-beam powder-bed additive manufacturing of metallic implants: a review on processes, materials and designs. *J Orthopaed Res* doi:10.1002/jor.23075
15. Yan C et al (2012) Evaluations of cellular lattice structures manufactured using selective laser melting. *Int J Mach Tools Manuf* 62:32–38
16. Fleck C, Eifler D (2010) Corrosion, fatigue and corrosion fatigue behaviour of metal implant materials, especially titanium alloys. *Int J Fatigue* 32(6):929–935
17. Zysset PKZ et al (1999) Elastic modulus and hardness of cortical and trabecular bone lamellae measured by nanoindentation in the human femur. *J Biomech* 32(10):1005–1012
18. Traini T et al (2008) Direct laser metal sintering as a new approach to fabrication of an isoelastic functionally graded material for manufacture of porous titanium dental implants. *Dent Mater* 24(11): 1525–1533
19. Van Bael S et al (2011) Micro-CT-based improvement of geometrical and mechanical controllability of selective laser melted Ti6Al4V porous structures. *Mater Sci Eng A* 528(24):7423–7431
20. Lin CY et al (2007) Structural and mechanical evaluations of a topology optimized titanium interbody fusion cage fabricated by selective laser melting process. *J Biomed Mater Res A* 83(2): 272–279
21. Wauthle R et al (2015) Effect of build orientation and heat treatment on the microstructure and mechanical properties of selective laser melted Ti6Al4V lattice structures. *Additive Manufac* 5:77–84
22. Wang YM et al (2007) Abnormal strain hardening in nanostructured titanium at high strain rates and large strains. *J Mater Sci* 42(5):1751–1756
23. Chichili DR, Ramesh KT, Hemker KJ (1998) The high strain-rate response of alpha-titanium: experiments, deformation mechanisms and modeling. *Acta Mater* 46(3):1025–1043
24. Gurao NP, Kapoor R, Suwas S (2011) Deformation behavior of commercially pure titanium at extreme strain rates. *Acta Mater* 59(9):3431–3446
25. Zhang J et al (2015) Effect of martensite morphology and volume fraction on strain hardening and fracture behavior of martensite-ferrite dual phase steel. *Mater Sci Eng A* 627:230–240
26. Sudarmadji N et al (2011) Investigation of the mechanical properties and porosity relationships in selective laser-sintered polyhedral for functionally graded scaffolds. *Acta Biomater* 7(2):530–537
27. Naing MW et al (2005) Fabrication of customised scaffolds using computer-aided design and rapid prototyping techniques. *Rapid Prototyp J* 11(4):249–259
28. Chua CK et al (2003) Development of a tissue engineering scaffold structure library for rapid prototyping. part 2: parametric library and assembly program. *Int J Adv Manuf Technol* 21:302–312
29. Yasa E. et al. (2010) Investigation of sectoral scanning in selective laser melting. in *ASME 2010 10th Biennial Conference on Engineering Systems Design and Analysis*. Istanbul, Turkey
30. Jhabvala J et al (2010) On the effect of scanning strategies in the selective laser melting process. *Virtual Phys Prototyping* 5(2): 99–109
31. Nemat-Nasser S, Guo WG, Cheng JY (1999) Mechanical properties and deformation mechanisms of a commercially pure titanium. *Acta Mater* 47(13):3705–3720
32. Loh LE et al (2015) Numerical investigation and an effective modelling on the selective laser melting (SLM) process with aluminium alloy 6061. *Int J Heat Mass Transf* 80:288–300
33. Gibson LJ, Ashby MF (1997) *Cellular solids: structures and properties*, 2nd edn. Cambridge University Press, New York
34. Cheng XY et al (2012) Compression deformation behavior of Ti-6Al-4 V alloy with cellular structures fabricated by electron beam melting. *J Mech Behav Biomed Mater* 16:153–162

35. Sing SL et al. (2014) Compression behavior of commercially pure titanium porous structures fabricated by selective laser melting, in RAPID 2014 Conference & Exposition. SME: Detroit, MI
36. Chlebus E et al (2011) Microstructure and mechanical behaviour of Ti-6Al-7Nb alloy produced by selective laser melting. Mater Charact 62:488–495